1989

A numerical study of wind forcing of eddies and jets in the California Current System

Batteen, Mary L.

Journal of Marine Research, 47, pp. 493-523, 1989
http://hdl.handle.net/10945/47160

Journal of Marine Research, 47, 493–523, 1989

A numerical study of wind forcing of eddies and jets in the California Current System

by Mary L. Batteen,[1] Robert L. Haney,[2] Terrance A. Tielking[1] and Philip G. Renaud[1]

ABSTRACT

A high-resolution, multi-level, primitive equation ocean model is used to examine the response to wind forcing of an idealized flat-bottomed oceanic regime along an eastern ocean boundary. A band of steady alongshore, upwelling favorable winds, either with or without alongshore variability, is used as forcing on both an f-plane and a β-plane. In each experiment a wind-driven equatorward coastal jet and a poleward undercurrent are generated. In time the coastal jet and undercurrent become unstable and lead to the development of eddies and jets with relatively strong onshore and offshore directed flows. The alongshore variation in alongshore wind stress plays a role in determining the location of eddy generation regions. A comparison of model results with available observations shows that the time-averaged model coastal jet and undercurrent are consistent in scale and magnitude with the observed data. Although the instantaneous eddies and jets are weaker than the corresponding observed features, they have horizontal scales typical of the observed scales. The results of this study support the hypothesis that steady wind forcing is one of several possible important generation mechanisms for eddies in the California Current System.

1. Introduction

The climatological mean California Current System (CCS) consists of four currents: the California Current, the California Undercurrent, the Davidson Current, and the Southern California Countercurrent (Hickey, 1979). The California Current is a broad, surface equatorward flow that can extend offshore to ~1000 km. The California Undercurrent is a subsurface poleward flow over the continental slope. The Davidson Current is defined as a surface poleward flow that occurs during the fall and winter north of Point Conception. The fourth current, the Southern California Countercurrent, is a surface poleward flow that occurs south of Point Conception and inshore of the Channel Islands in the Southern California Bight.

Recent observations have shown that, superimposed on the broad, slow (~10 cm s^{-1}), climatological mean flow in the CCS are highly energetic, mesoscale

1. Department of Oceanography, Naval Postgraduate School, Monterey, California, 93943-5000, U.S.A.
2. Department of Meteorology, Naval Postgraduate School, Monterey, California, 93943-5000, U.S.A.

eddies and meandering jets (Bernstein *et al.*, 1977; Mooers and Robinson, 1984; Rienecker *et al.*, 1985, 1988). The meanders, which have wavelengths of up to several hundred kilometers, can intensify over several months and be "cut off," becoming isolated eddies (Bernstein *et al.*, 1977). Strong baroclinic jets with peak velocities of $\sim$80 cm s^{-1} are embedded in this field of cyclonic and anticyclonic eddies. These jets are $\sim$70 km wide at the surface, extend to at least 100 m depth, and have offshore excursions of several hundred kilometers (Mooers and Robinson, 1984; Rienecker *et al.*, 1985; Flament *et al.*, 1985; Kosro and Huyer, 1986).

The dynamical processes responsible for the generation and evolution of these intense and complex eddy and jet patterns in the CCS have yet to be fully identified. A possible generative mechanism arises from the baroclinic and/or barotropic instability of the mean coastal California Current System which, during the upwelling season (from $\sim$ April to October), consists of an equatorward-flowing surface current or coastal jet with mean speeds of $\sim$10 to 30 cm s^{-1} overlying a poleward-flowing undercurrent with a mean speed of $\sim$10 cm s^{-1} (Hickey, 1979; Chelton, 1984; Huyer and Kosro, 1987).

Both baroclinic and barotropic instabilities have been shown to generate eddies and jets in the northeast Pacific (Wright, 1980). Baroclinic instability is an important mechanism for eddy generation off Vancouver Island (Emery and Mysak, 1980; Thomson, 1984), and off the coast of Oregon and northern California (Ikeda and Emery, 1984). In particular, Ikeda and Emery (1984) have hypothesized that current meanders are triggered by alongshore variations in the coastline (capes) and grow as a result of the baroclinic instability of the coastal, equatorward, near-surface jet ($\sim$40 km wide and associated with coastal upwelling) and the poleward California Undercurrent. As these unstable meanders intensify, they carry the cool, upwelled water offshore and are often cut off, creating pairs of isolated eddies or "vortex pairs" consisting of a cyclonic and an anticyclonic eddy (Bernstein *et al.*, 1977). Evidence for barotropic instability as a viable mechanism is still forthcoming, although one case of eddy-eddy-jet interaction observed by the OPTOMA (Ocean Prediction Through Observations, Modeling and Analysis) Program in the summer of 1983 showed characteristics of barotropic instability (Robinson *et al.*, 1984). There is evidence for both processes occurring off Vancouver Island where a cyclonic eddy was formed by a primary contribution from baroclinic instability and an additional, yet secondary, contribution from barotropic instability (Thomson, 1984).

The role of wind forcing in the generation of eddies and jets in the CCS has not been systematically investigated and may be the most important generation mechanism for eddy and jet formation. Satellite infrared imagery has shown evidence of eddies and jets in the CCS during periods of winds favorable for upwelling. These observations provide evidence for wind forcing as a possible important mechanism for eddy and jet formation. Eddies and jets could be caused by either a response to the seasonal mean wind field or to short-lived, strong wind events occurring during the upwelling season.

In this study, a high-resolution, multi-level, primitive equation ocean model is used to examine the response to climatological wind forcing of an idealized oceanic regime along an eastern ocean boundary. A band of steady alongshore winds, either with or without alongshore variability, is used as forcing on both an f-plane and a β-plane. It is seen in all experiments that both a wind-driven, equatorward coastal jet and a poleward undercurrent develop, which become unstable, resulting in the generation of eddies and jets. It is also seen that the alongshore variation in wind stress can play a role in determining the location of eddy generation regions.

2. Model description and specific experimental conditions

a. Model equations. The numerical model used in this research was developed by Haney (1985), modified by Batteen (1989), and is a multi-level, primitive equation (PE) model. The model uses the hydrostatic, rigid lid, β-plane and Boussinesq approximations. The governing equations are as follows:

$$\frac{du}{dt} = \frac{-1}{\rho_o}\frac{\partial p'}{\partial x} + fv - A_m\nabla^4 u + K_m\frac{\partial^2 u}{\partial z^2} + \delta_d(u) \tag{1}$$

$$\frac{dv}{dt} = \frac{-1}{\rho_o}\frac{\partial p'}{\delta y} - fu - A_m\nabla^4 v + K_m\frac{\partial^2 v}{\partial z^2} + \delta_d(v) \tag{2}$$

$$w = -\int_{-H}^{z}\left(\frac{\partial u}{\partial x} + \frac{\partial v}{\partial y}\right)d\xi \tag{3}$$

$$p' = \int_z^o \rho g\, d\xi - \frac{1}{H}\int_{-H}^{o}\left[\int_z^o \rho g\, d\xi\right]dz \tag{4}$$

$$\rho = \rho_o\,(1 - \alpha\,(T - T_o)) \tag{5}$$

$$\frac{dT}{dt} = -A_H\nabla^4 T + K_H\frac{\partial^2 T}{\partial z^2} + Q_s + \delta_d(T). \tag{6}$$

In the above equations, t is time, (x, y, z) is a right-handed cartesian coordinate system with x pointing toward shore, y alongshore, and z upward. The corresponding velocity components are (u, v, w), T is temperature, ρ is density and p' is the departure of the pressure from the vertically averaged pressure. In Eqs. (3) and (4), ξ is a dummy variable of integration. Eq. (4) includes the assumption that the depth-averaged pressure is a constant (assumed zero); i.e., the barotropic mode is ignored in this study. Eq. (5) assumes that density is a function of temperature only, consistent with the region of the CCS being modeled (e.g., the temperature, salinity and density figures from CalCOFI Line 60, i.e., pp. 107, 115 and 123 of Lynn *et al.* (1982), show that density is primarily a function of temperature). Although salinity may be a good tracer

for water masses in the CCS (Huyer and Kosro, 1987), it is not essential for a zero-order description of the CCS, since there are no major salinity sources or sinks (such as major rivers) in the region being modeled. In (6), $Q_s = \partial S/\rho_o C \partial z$ is the heating due to solar radiation, with

$$S = S_o\,(Re^{z/z_1} + (1 - R)e^{z/z_2}). \tag{7}$$

Here S_o is the downward flux of solar radiation at the surface (see below), $R = .62$ is the fraction of solar radiation absorbed in the upper few meters ($z_1 = 1.5$ m) and $(1 - R) = 0.38$ is the fraction that penetrates to somewhat deeper levels ($z_2 = 20$ m) as given by Paulson and Simpson (1977). The terms $\delta_d(u)$, $\delta_d(v)$ and $\delta_d(T)$ represent the vertical turbulent mixing of heat and momentum by a dynamic adjustment mechanism. This adjustment, a generalization of the convective adjustment mechanism, is based on the assumption of a critical Richardson number, and it serves to maintain dynamic stability in the water column (Adamec *et al.*, 1981).

The boundary conditions at the top ($z = 0$) of the model ocean are:

$$K_m \frac{\partial u}{\partial z} = 0 \tag{8a}$$

$$K_m \frac{\partial v}{\partial z} = \tau/\rho_o \tag{8b}$$

$$K_H \frac{\partial T}{\partial z} = -Q_B \tag{8c}$$

$$w = 0, \tag{8d}$$

and at the bottom ($z = -H$) they are

$$K_m \frac{\partial u}{\partial z} = C_D\,(u^2 + v^2)^{1/2}\,(u \cos\gamma - v \sin\gamma) \tag{9a}$$

$$K_m \frac{\partial v}{\partial z} = C_D\,(u^2 + v^2)^{1/2}\,(v \cos\gamma - u \sin\gamma) \tag{9b}$$

$$K_H \frac{\partial T}{\partial z} = 0 \tag{9c}$$

$$w = 0. \tag{9d}$$

In (8b), τ is the alongshore component of the surface stress which is varied in different experiments as described below. In (8c), Q_B is the net upward flux of longwave radiation, sensible and latent heat across the sea surface which is described below. In (9a, b), $C_D = 1.225 \times 10^{-3}$ is a bottom drag coefficient and $\gamma = 10°$ is a geostrophic inflow angle (Weatherly, 1972). The bottom stress in (9a, b) represents one of the simplest possible parameterizations of a bottom Ekman layer. Table 1 provides other

Table 1. Values of constants used in the model.

	Value	Definition
C	0.958 cal gm^{-1} $(°K)^{-1}$	specific heat of sea water
C_D	1.225×10^{-3}	bottom drag coefficient
T_0	278.2°C	constant reference temperature
ρ_a	1.23×10^{-3} gm cm^{-3}	density of air
ρ_o	1.0276 gm cm^{-3}	density of sea water at T_0
α	2.01×10^{-4} $(°K)^{-1}$	thermal expansion coefficient
K	10	number of levels in vertical
Δx	8×10^5 cm	cross-shore grid spacing
Δy	1×10^6 cm	alongshore grid spacing
D	4.5×10^5 cm	total ocean depth
Δt	800 s	time step
f_o	0.93×10^{-4} s^{-1}	mean Coriolis parameter
g	980 cm s^{-2}	acceleration of gravity
A_M	2×10^{17} cm^4 s^{-1}	biharmonic momentum diffusion coefficient
A_H	2×10^{17} cm^4 s^{-1}	biharmonic heat diffusion coefficient
K_M	0.5 cm^2 s^{-1}	vertical eddy viscosity
K_H	0.5 cm^2 s^{-1}	vertical eddy conductivity

symbols in the model equations as well as values of constants used throughout this study.

b. Domain size and resolution. The domain of the model is the rectangular region extending from approximately 124 to 130W and from 36.5 to 42.5N, covering an area of 6° longitude by 6° latitude (Fig. 1). The region extends approximately 500 km offshore from the west coast of North America, and it spans the California coastline from Point Sur in the south to Cape Blanco in the north (640 km). The horizontal resolution of the model is 8 km in the cross-shore direction and 10 km in the alongshore direction. This horizontal grid resolution should allow realistic spatial resolution of mesoscale features in the CCS, which have typical wavelengths of the order of 100 km (Breaker and Mooers, 1986). Although there are significant variations in the coastline and ocean depth in the CCS, these variations are omitted in the model in order to focus on the role of steady wind forcing in the generation of eddies.

c. Finite difference scheme. In the horizontal, a space-staggered *B*-scheme (Arakawa and Lamb, 1977; Batteen and Han, 1981) is used. There are 10 layers in the vertical, separated by constant z-levels placed at depths of 13, 46, 98, 182, 316, 529, 870, 1416, 2283 and 3656 m.

d. Heat and momentum diffusion. The model uses biharmonic lateral momentum and heat diffusion with the choice of coefficients listed in Table 1. Holland and Batteen (1986) have shown that Laplacian lateral heat diffusion can diminish the baroclinic

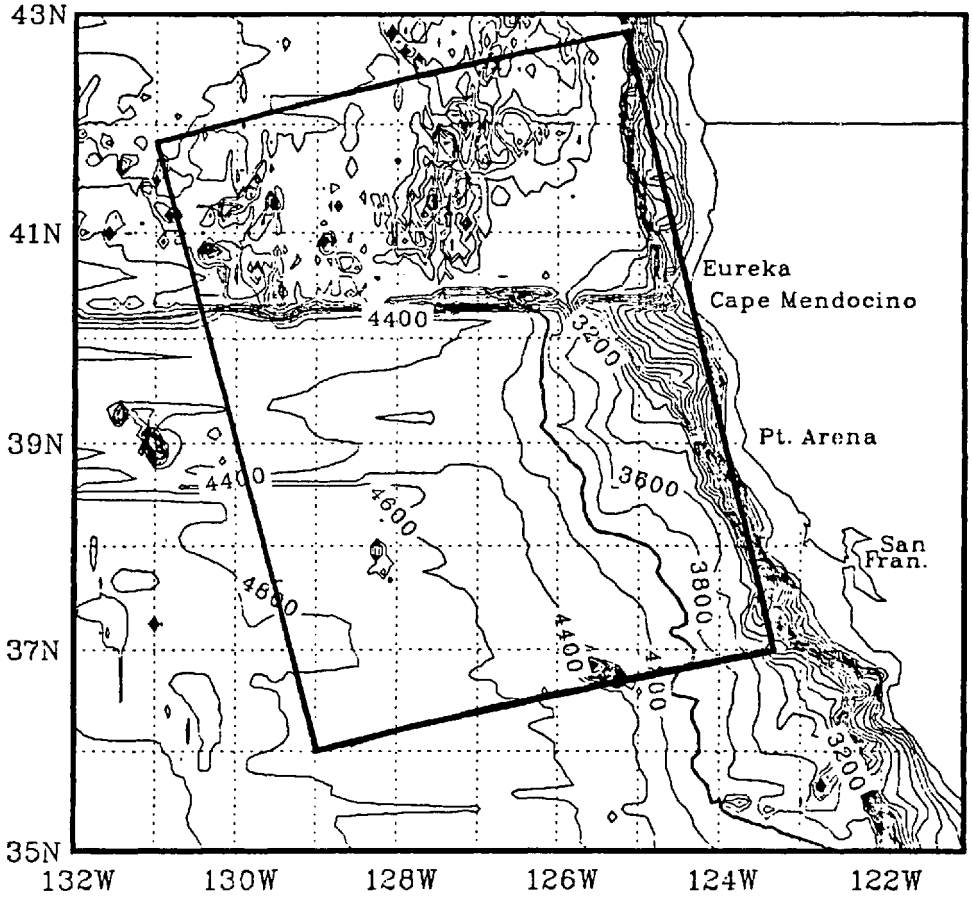

Figure 1. Study domain. The rectangle represents the primitive equation (PE) model domain. Bathymetry in meters, contour interval is 200 m.

signal associated with mesoscale processes, making it less likely that baroclinic instability processes can exceed the diffusive damping. Since biharmonic diffusion is scale selective and acts predominantly on scales smaller than those of eddies (Holland, 1978), the use of biharmonic, rather than Laplacian lateral diffusion, along with the appropriate coefficients, should allow mesoscale eddies to be generated via baroclinic and/or barotropic instability processes.

e. Wind forcing. Using ship observations in one-degree square areas, Nelson (1977) compiled a complete description of monthly mean wind stress off the west coast of the United States. These historical marine wind stress fields were used to determine the wind forcing of the PE model. The wind stress data of Nelson (1977) for the summer months show that the mean wind stress has an alongshore, equatorward component, implying conditions generally favorable for coastal upwelling. To investigate the role of

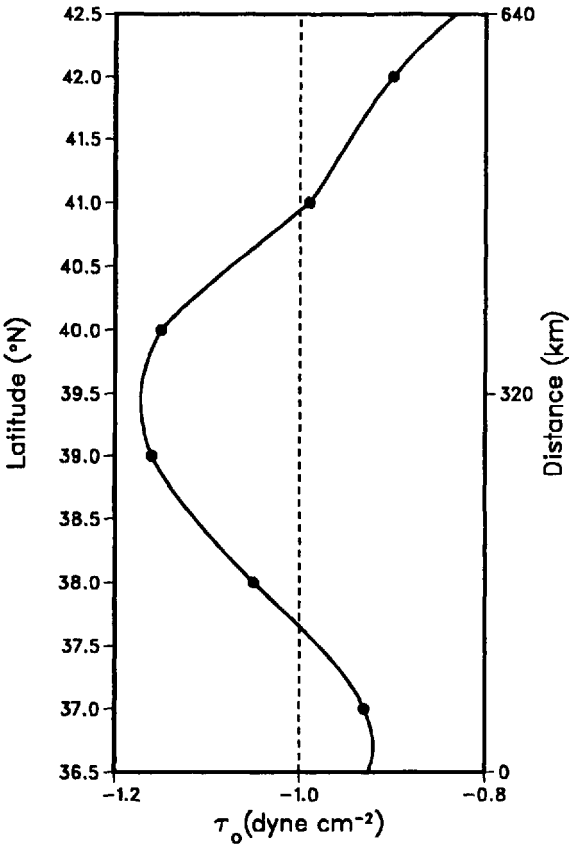

Figure 2. Wind stress (τ_o) versus latitude and alongshore distance. The dashed line represents the uniform alongshore component of the model wind stress used in Experiments 1 and 2, while the solid line with dots represents the variable alongshore component of the model wind stress used in Experiments 3 and 4.

this wind stress as a mechanism for eddy and jet formation, the alongshore component of the wind stress field during summer (June–August) was averaged zonally and meridionally in the area of the model domain. The resulting equatorward wind stress forcing of 1 dyne cm^{-2} (equatorward mean wind of ~8.3 ms^{-1}) was used in the model for the experiments with constant wind forcing (Experiments 1 and 2).

In addition to an equatorward wind stress for the summer months, the wind observations of Nelson (1977) show that the mean equatorward wind stress can vary by 20–30% over only several degrees of latitude. Maximum values of surface wind stress occur off Cape Mendocino, where characteristic values can approach 1.2 dynes cm^{-2} (Fig. 2) over a distance which extends 500 km in the offshore direction. It is feasible that alongshore variations in the alongshore wind field can result in the development of a complex system of currents and contribute to some of the spatial seasonal variability

of the CCS. To examine the role of alongshore variations in the wind in the area off Cape Mendocino, the climatological alongshore wind stress from Nelson (1977) was zonally averaged over the model domain for the summer season (Fig. 2) and used as the forcing in Experiments 3 and 4. The alongshore variations in the zonally averaged wind stress show a maximum southward stress of $\sim$1.2 dyne cm^{-2} at 39.5N, which could serve to generate eddies preferentially at this latitude.

f. Surface thermal forcing. Like all major eastern boundary current systems, the CCS is a region of net annual heat gain (Nelson and Husby, 1983). This heat gain occurs because of relatively low cloud cover (compared with farther offshore), reduced latent heat flux, and downward sensible heat flux due to the presence of cold upwelled water during summer. To focus this study on wind forcing as a possible mechanism for the generation of thermal variability in the CCS, the surface thermal forcing in the model was highly simplified. The solar radiation at the sea surface, S_o, was specified to be the summer-mean and CCS-mean value from Nelson and Husby (1983). On the other hand, the sum of the net longwave radiation, latent and sensible heat fluxes, Q_B, was computed during the model experiments from standard bulk formulas (Haney *et al.*, 1978) using the summer- and CCS-mean value of alongshore wind (above), cloud cover, relative humidity, air temperature and model-predicted sea surface temperature. In all the experiments shown below, the initial sea surface temperature was chosen so that the total heat flux across the sea surface, $S_o - Q_B$, was zero at the initial time. Therefore, the only surface heat flux forcing in the experiments was that which developed in Q_B as a result of (wind-forced) fluctuations in the sea surface temperature. As discussed in Haney (1985), such a surface thermal forcing damps the sea surface temperature fluctuations to the atmosphere on a time scale of the order of 100 days. Consequently, sea surface temperature fluctuations that develop due to wind forcing should be observed long before they are damped by the computed surface heat flux.

g. Boundary conditions. The eastern boundary, representing the west coast of North America, is modeled as a straight, vertical wall. A no-slip condition on the tangential velocity is invoked at the coastline.

The northern, southern and western boundaries are open using a modified version of the radiation boundary conditions of Camerlengo and O'Brien (1980). Whereas no problems were encountered in the use of these open boundary conditions for unforced cases as in Batteen (1989), the results are not realistic for wind-forced cases if the forcing is applied not only in the interior but also on both the northern and southern open boundaries of the model domain. McCreary (1981) showed that if a uniform wind stress is used, a steady alongshore current will result that is too strong, too deep and directed equatorward at all depths. To generate a realistic undercurrent, he recommended the use of wind band forcing of the form:

$$\tau = \tau_o Y(y), \tag{10}$$

where τ_o is the actual wind stress (which may depend on y, as in Fig. 2), and $Y(y)$ is an imposed latitudinal variation that is needed to make $\tau = 0$ on the northern and southern boundaries. Following McCreary *et al.* (1987), we have also imposed a band of meridional wind forcing in the interior of the domain away from both the northern and southern boundaries. The wind band function is given by

$$Y(y) = \begin{cases} 1 & 37° < y < 42° \\ 0 & \text{otherwise.} \end{cases} \tag{11}$$

The use of wind band forcing $Y(y)$, while somewhat artificial in form, allows for the propagation of coastal Kelvin waves which thereby establish the alongshore pressure gradient field, with the result that a surface-trapped coastal jet and a relatively realistic undercurrent are generated. In addition, we extend the results of McCreary *et al.* (1987) by showing that the jet and undercurrent are unstable and as a result, eddies and jets are generated.

h. Initial conditions. The initial mean stratification used in all experiments was an exponential temperature profile with a vertical length scale of $h = 450$ m. The exact form was:

$$T(z) = T_B + \Delta T e^{z/h}, \tag{12}$$

where $T_B = 2°C$ is the temperature at great depth and $\Delta T = 13°C$ is the increase in temperature between the bottom of the ocean and the surface. This temperature profile was derived from available CCS observations used to support the Dynalysis of Princeton model (Blumberg and Mellor, 1987) and has been considered by Blumberg and Mellor (1987) to be representative of the long-term, mean climatological temperature stratification for the CCS region as a whole.

3. Results

In the following sections we examine the oceanic response to steady winds, either with or without alongshore variability, on both an f-plane and a β-plane. Experiments 1 and 2 use a band of constant wind stress on an f-plane and a β-plane, respectively, while Experiments 3 and 4 use a band of alongshore-varying wind stress on an f-plane and a β-plane, respectively.

a. Experiment 1 (constant wind stress on an f-plane). Experiment 1 was run on an f-plane with a constant Coriolis parameter of $f_o = 9.3 \times 10^{-5}$ s^{-1} based on the mean latitude of the domain. The wind forcing (τ_o) for this experiment was constant (1 dyne cm^{-2}), both in the alongshore and cross-shore directions and steady for a 90-day period.

The model was forced with full magnitude winds and, as expected, inertial oscillations of near-surface ocean currents developed. These oscillations were damped

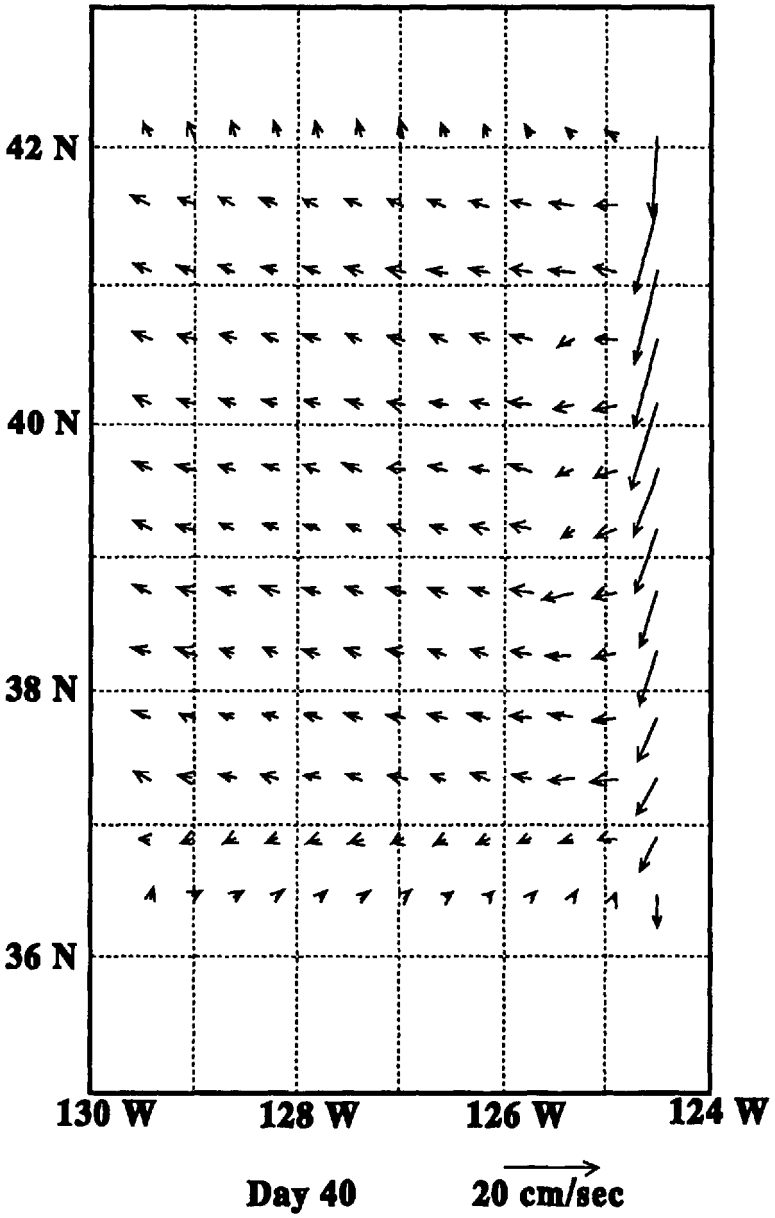

Figure 3. Surface current vectors for Experiment 1 at day 40.

after several inertial periods, leaving quasi-steady offshore Ekman transport to the right of the wind stress, as shown at day 40 in Figure 3.

The subsequent offshore progression of cold water (Figs. 4a and 4b) is caused by the cold, upwelled water replacing the coastal waters. Surface temperature gradients near the coast are ~0.031°C km^{-1} and increase slightly with time throughout the duration of the experiment.

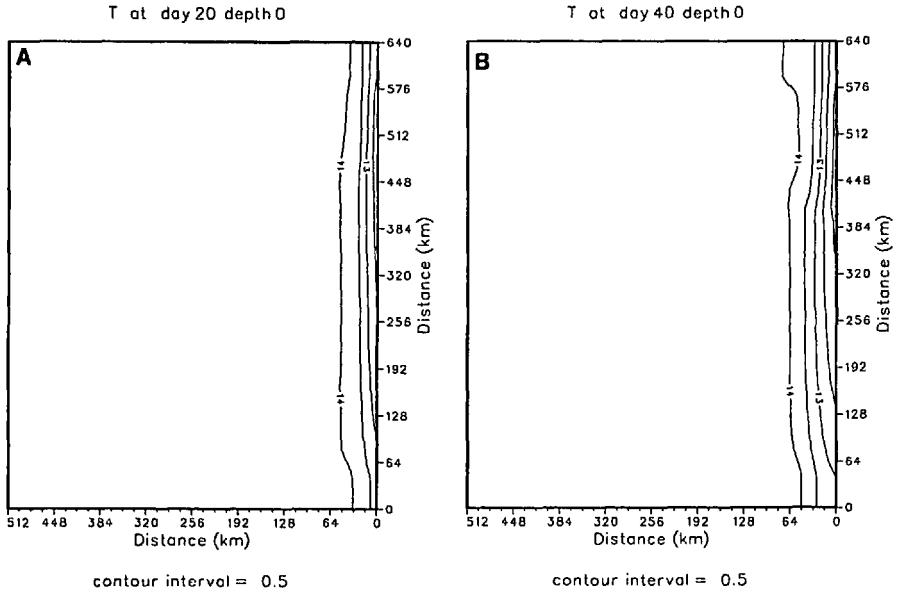

Figure 4. Surface contours of temperature (°C) for Experiment 1 at (A) day 20 and (B) day 40. Contour interval is 0.5°C.

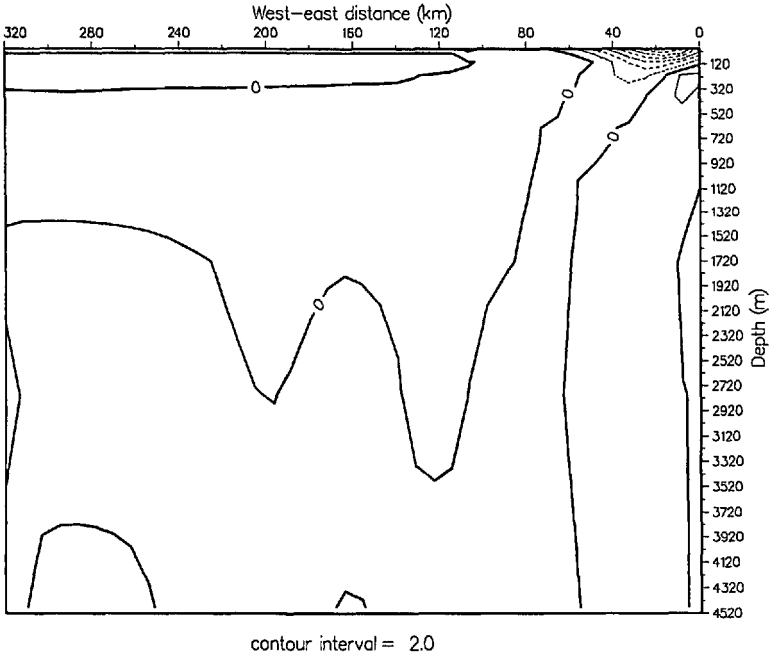

Figure 5. Vertical cross-shore section of meridional (v) velocity (cm s^{-1}) for Experiment 1 at day 40. Contour interval is 2.0 cm s^{-1}. Dashed contours denote equatorward velocities. The vertical cross-section was alongshore-averaged.

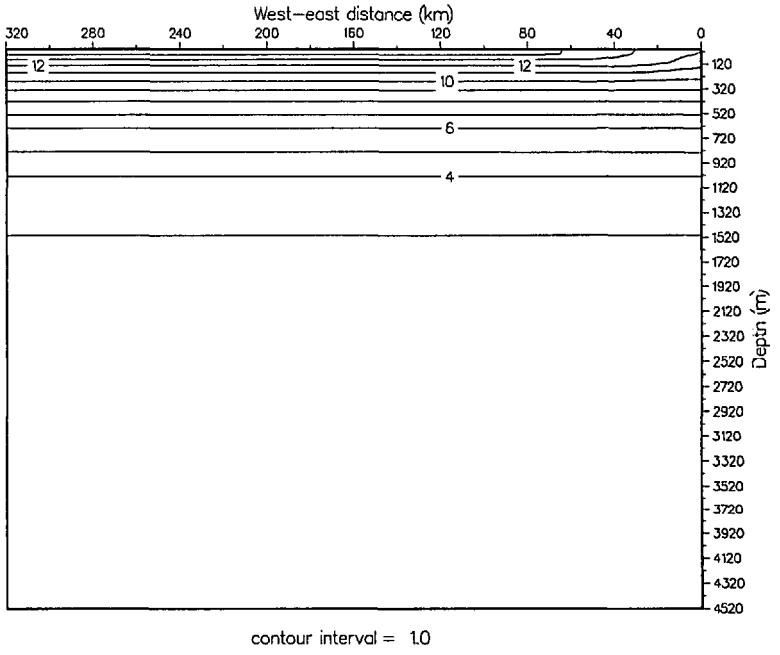

Figure 6. Vertical cross-shore section of temperature (°C) for Experiment 1 at day 40. Contour interval is 1.0°C. The vertical cross-section was alongshore-averaged.

The steady, equatorward wind forcing resulted in an equatorward, surface coastal jet (Fig. 5) with a maximum velocity of ~14 cm s^{-1} by day 40. This nearshore surface flow is geostrophic and in balance with the density field according to the thermal wind equation. Gill (1982) showed that on an *f*-plane the coastal jet should be confined to within the first internal Rossby radius of deformation of the coast. This radius is ~30 km for the model domain, as calculated by the method of Feliks (1985). The coastal jet axis seen in Figure 5 is ~16 km from the coast, has a maximum offshore extent of ~45 km and extends to ~200 m depth. This coastal jet development agrees well with the steady wind forcing results of McCreary *et al.* (1987).

A weak, poleward current of ~2 cm s^{-1} is also seen in Figure 5 below the surface current at a depth of ~200–370 m. The offshore extent of the undercurrent is confined to ~10 km of the coast. McCreary (1981) found that a poleward undercurrent can develop as a result of an alongshore pressure gradient established via an alongshore variation in the wind stress and the poleward propagation of Kelvin waves. Vertical mixing of heat and momentum was also necessary. McCreary (1981) described the sequence of events on an *f*-plane with suddenly imposed winds. First, offshore Ekman transport occurred in the area of the applied wind. Next, an upwelling signal propagated rapidly poleward as a coastal Kelvin wave. As the Kelvin wave passed, a coastal jet was set up and provided a source of water for the offshore Ekman transport.

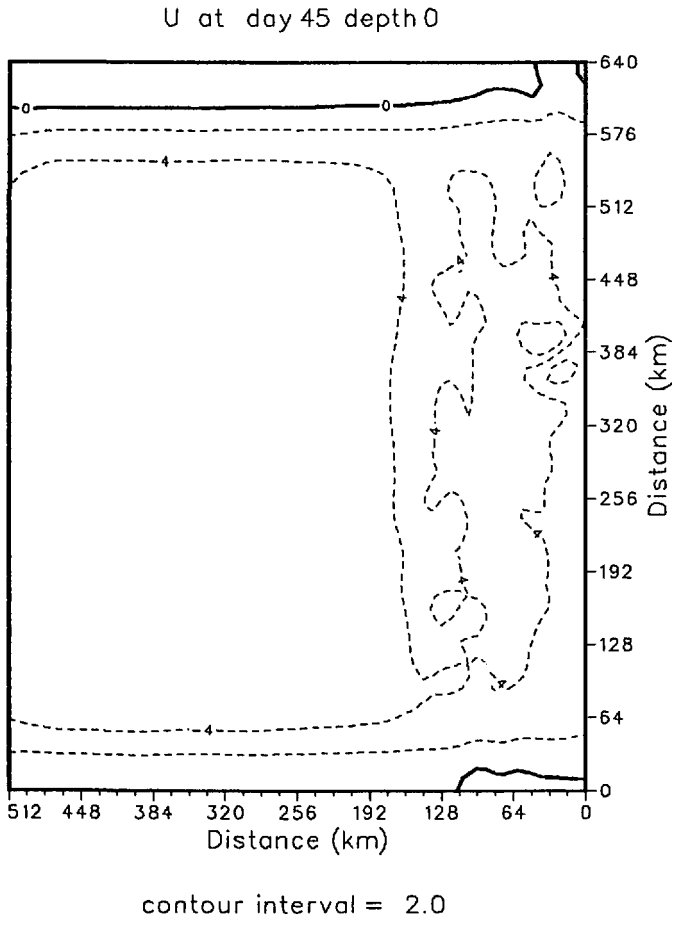

Figure 7. Surface zonal (u) velocity (cm s^{-1}) for Experiment 1 at day 45. Contour interval is 2.0 cm s^{-1}. Dashed contours denote offshore velocities.

Philander and Yoon (1982) found that Kelvin waves also introduced an undercurrent which reduced the intensity of coastal upwelling, but did not modify the zonal velocity perpendicular to the coast.

The vertical and offshore extent of the colder, upwelled waters is depicted in the vertical cross-shore section of temperature (Fig. 6). The initial conditions of a horizontally uniform temperature field have been changed by the presence of colder, upwelled water near the coast. Consequently, a rise of isotherms, consistent with upwelling, above ~200 m can be seen. The near-surface upwelled water extends ~70 km offshore. These results are consistent with McCreary (1981), who found that upwelling did not reach deep depths, but was confined to above the core of the undercurrent. At around day 45 of the experiment, the first evidence of developing ocean eddies can be seen (Fig. 7) as perturbations in the zonal current near the coast at

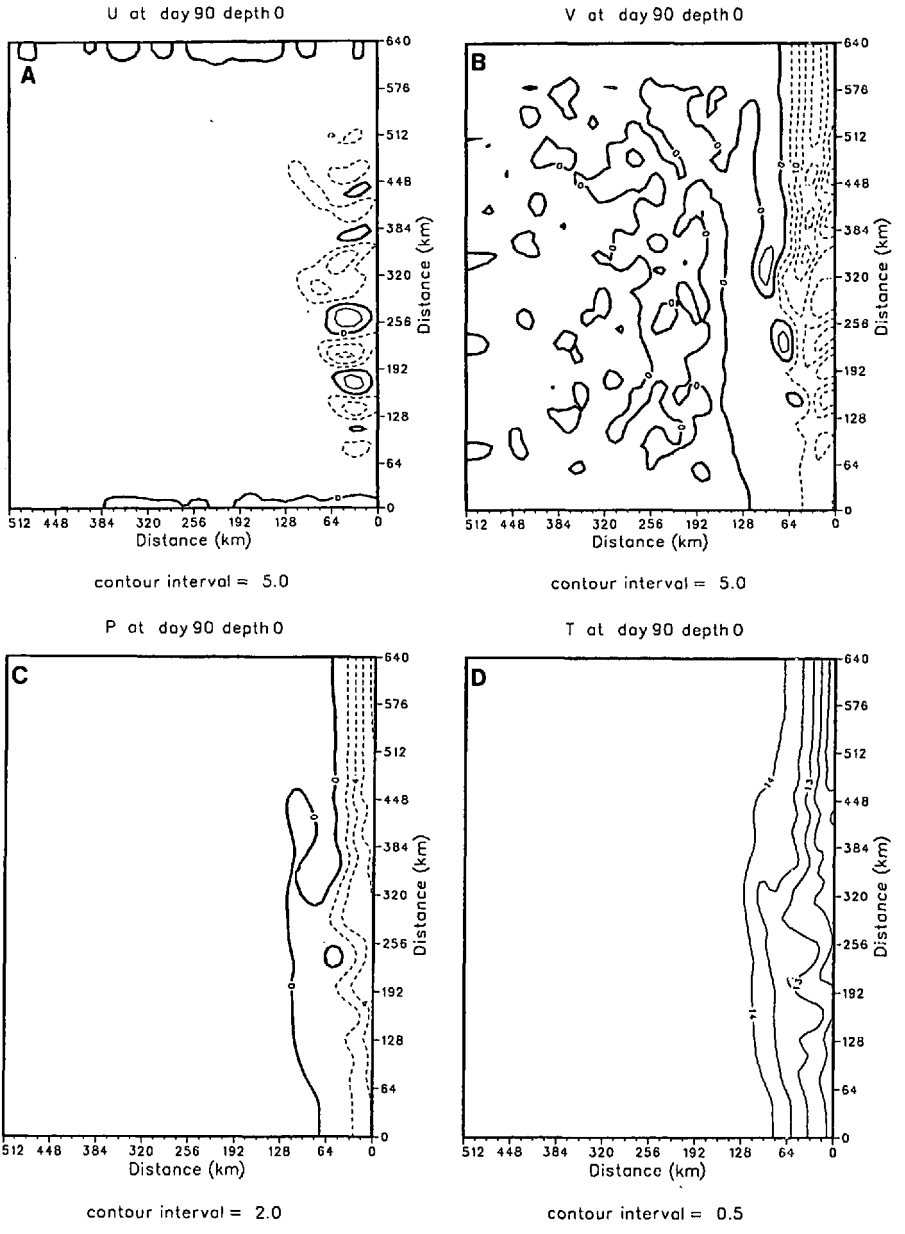

Figure 8. Surface isopleths for Experiment 1 at day 90 of (A) zonal (u) velocity (cm s^{-1}), (B) meridional (v) velocity (cm s^{-1}), (C) dynamic height (cm) relative to 2400 m and (D) temperature (°C). Contour interval is 5.0 cm s^{-1} for (A) and (B), 2.0 cm for (C) and 0.5°C for (D). Dashed lines denote offshore velocities in (A), equatorward velocities in (B) and negative (relative to 2400 m) values in (C).

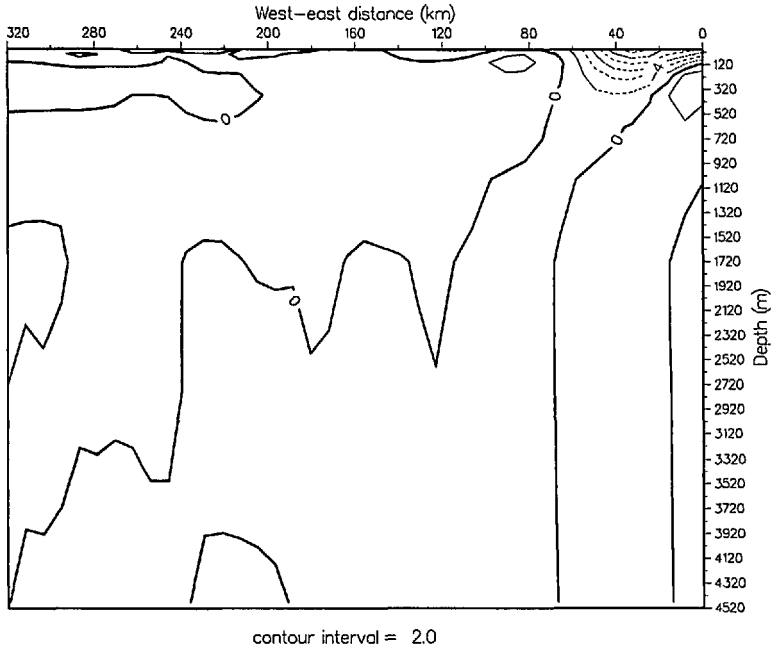

Figure 9. Same as Figure 5 except at day 90.

$y \sim 384$ km. As will be seen in Section 4, these eddies develop due to the presence of the coastal jet, which becomes unstable. These mesoscale features continued to develop near the center of the model domain along the coast (between $y \sim 160$–448 km). The instantaneous zonal velocity field at day 90 (Fig. 8a) shows that the alongshore wavelength for these eddies is ~75 km with maximum zonal velocities ~15 cm s^{-1}. The maximum instantaneous velocity of the coastal jet at day 90 (Fig. 8b) is greater than 20 cm s^{-1} with the core at about 30 km offshore, and the maximum offshore extent ~64 km.

The cross-shore section of the meridional velocity at day 90 (Fig. 9) shows that the poleward undercurrent extends to ~16–18 km offshore, from ~150 m to 600 m depth, and has a maximum core velocity of ~2 cm s^{-1}. The surface coastal jet axis is shown to extend to ~32 km offshore, and extends to ~350 m depth offshore of the undercurrent.

The surface pressure field, shown in Figure 8c at day 90, was calculated as the hydrostatic pressure field relative to 2400 m depth. The dynamic height slopes downward toward the coast, as expected. In addition, there is an anticyclonic eddy 50 km offshore at $y \sim 250$ km. A comparison of Figure 8c with Figure 8d, which shows the sea surface temperature field at day 90, shows that the isotherm perturbations align with the offshore/onshore geostrophic flow of the eddies. These results are consistent with CCS observations of cold, seaward flows, called squirts (Davis, 1985).

b. Experiment 2 (uniform wind stress on a β-plane). Experiment 2 used the same parameters and forcing mechanisms as in Experiment 1, but used a β-plane rather than an f-plane. The Beta effect allows the existence of freely propagating planetary waves, i.e., Rossby waves (Gill, 1982). Due to the Beta effect, the surface coastal jet does not necessarily have to be confined to within a Rossby radius of deformation of the coast (McCreary *et al.*, 1987). The offshore radiation of Rossby waves, according to McCreary (1981), can contribute to the generation of an alongshore pressure gradient field, which can cause a poleward undercurrent to develop. If no vertical mixing is allowed, the Beta effect can also intensify the undercurrent and advect the coastal currents offshore.

In Experiment 2, the first evidence of developing eddies was seen in the zonal velocity field (Fig. 10) at ~day 40. The perturbations were generated a little farther to the north in the β-plane experiment than in the f-plane experiment. Surface contour plots of instantaneous velocity, temperature and dynamic height at day 90 are shown in Figure 11. The maximum zonal velocity (Fig. 11a) reached is ~15 cm s^{-1} coinciding with the generation of an anticyclonic eddy at $y \sim 224$ km (Fig. 11c). The 13.5°C temperature pool in the same area (Fig. 11d) is associated with the warm core of this anticyclone.

The surface equatorward coastal jet (Fig. 11b) has maximum velocities of ~10–15 cm s^{-1} which are located offshore at ~56 km. This is approximately 5 cm s^{-1} weaker and 25 km farther offshore than the results of Experiment 1. A comparison of the coastal jet and undercurrent region in this experiment (Fig. 12) at day 90 and that in Experiment 1 (Fig. 9) showed that in this experiment the coastal jet was weaker and shallower offshore and the undercurrent wider and stronger. The maximum offshore extent of the undercurrent was ~30 km, which was ~15 km farther offshore than in Experiment 1.

The intensification and widening of the undercurrent must be due to the Beta effect. The detensification and shallowing of the coastal jet offshore compared to the jet in Experiment 1 must also be due to the Beta effect. These results are consistent with Hurlburt and Thompson (1973) and McCreary *et al.* (1987).

c. Experiment 3 (alongshore-varying wind stress on an f-plane). Experiment 3 was similar to Experiment 1 with the exception of an imposed meridional variation in the alongshore wind stress (τ_o) with maximum at $y \sim 320$ km, as shown in Figure 2 and discussed in Section 2.

The initial results of Experiment 3 were quite similar to Experiment 1. After further evolution of the eddy field, as seen in Figure 13, the core of the equatorward coastal jet (Fig. 13b) is centered ~32 km offshore with a maximum velocity of ~20 cm s^{-1}. A notable difference from Experiment 1 was that no eddies developed north of ~385 km in Experiment 3 (compare Figs. 8a and 8c with Figs. 13a and 13c). This was probably due to the maximum wind stress occurring south of this region. The zonal (u) velocities

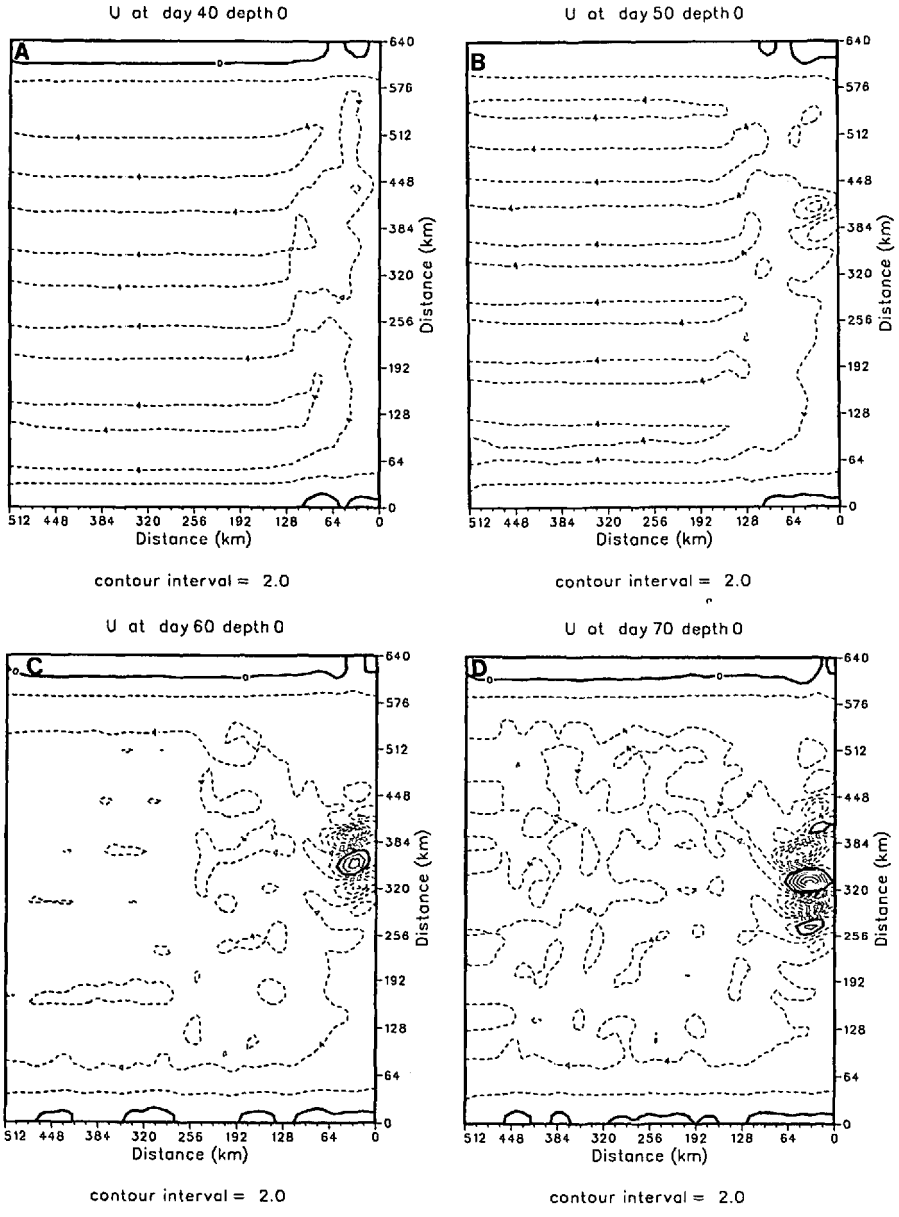

Figure 10. Surface isopleths of zonal (u) velocity (cm s^{-1}) for Experiment 2 at (A) day 40, (B) day 50, (C) day 60 and (D) day 70. Contour interval is 2.0 cm s^{-1}. Dashed contours denote offshore velocities.

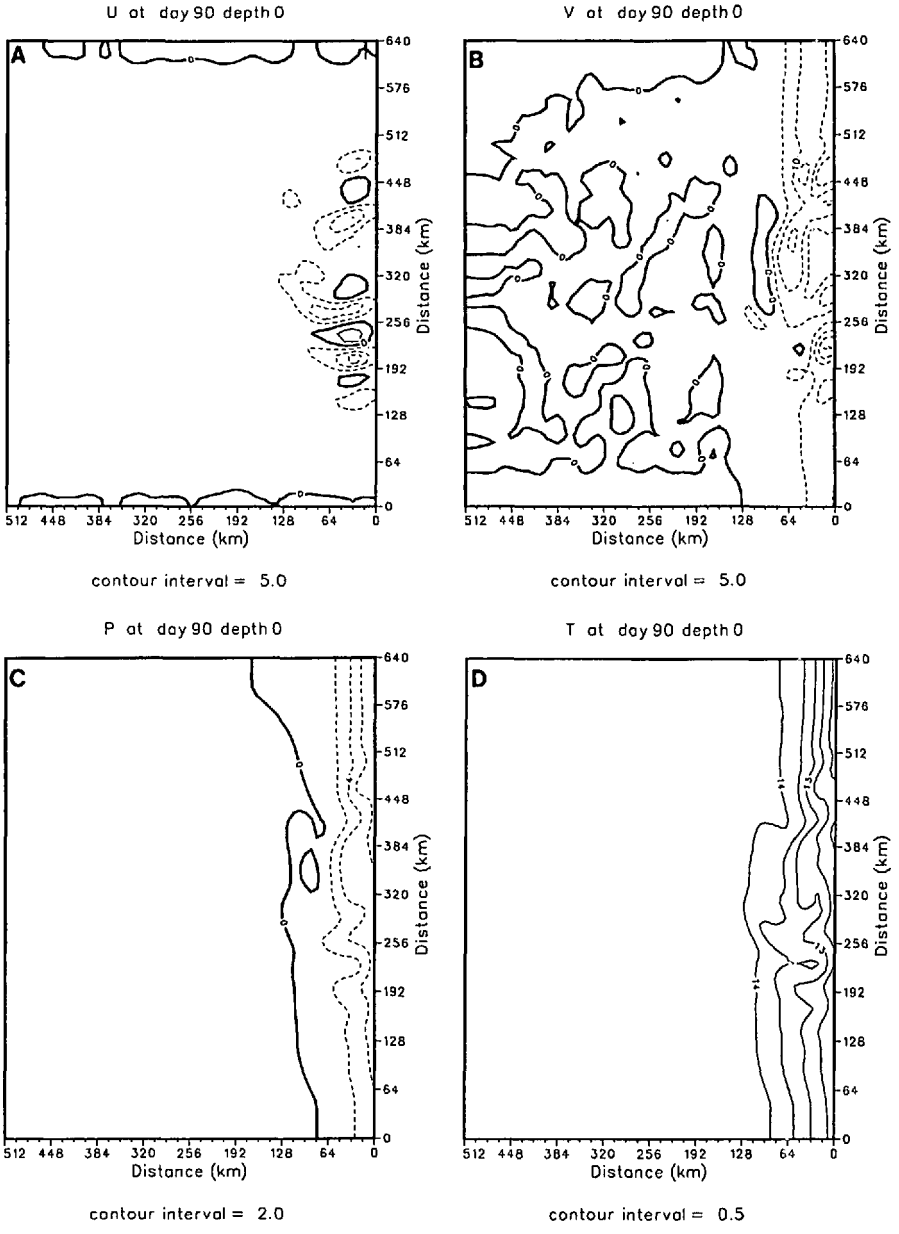

Figure 11. Surface isopleths of (A) zonal (u) velocity (cm s^{-1}), (B) meridional (v) velocity (cm s^{-1}), (C) dynamic height (cm) relative to 2400 m and (D) temperature (°C) for Experiment 2 at day 90. Contour interval is 5.0 cm s^{-1} for (A) and (B), 2.0 cm for (C), and 0.5°C for (D). Dashed contours denote offshore velocities in (A), equatorward velocities in (B) and negative values relative to 2400 m in (C).

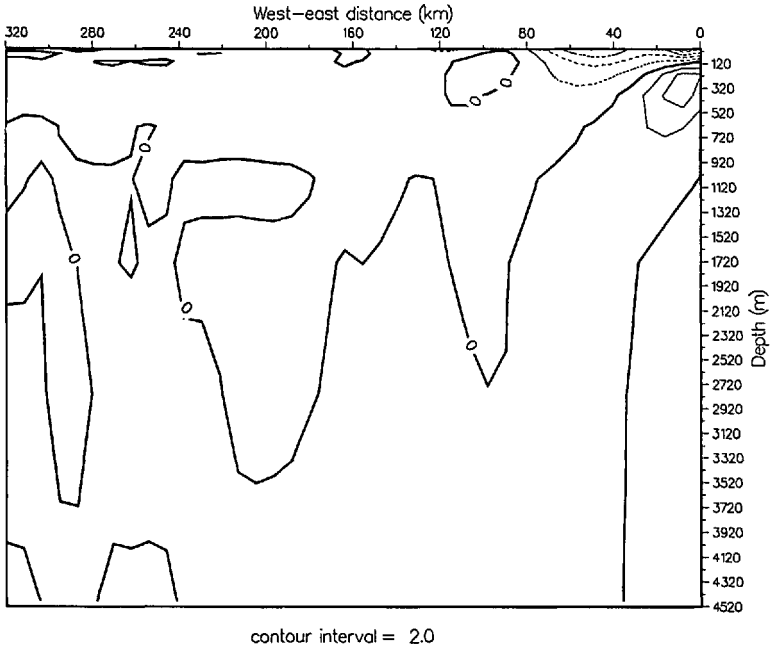

Figure 12. Same as Figure 9 except for Experiment 2.

(Fig. 13a) of ~5 cm s^{-1} well seaward of the coast are associated with stronger Ekman transport in response to the stronger alongshore varying wind stress at that latitude (see Fig. 2), as expected. Temperature perturbations (Fig. 13d) associated with the meandering features also occurred farther to the south. This experiment showed that the alongshore variation in the mean alongshore wind stress can modify the location of the eddy development region. In particular, eddies tend to be generated preferentially in, and downstream of, the region of maximum alongshore wind stress.

d. Experiment 4 (alongshore-varying wind stress on a β-plane). This experiment used the same forcing parameters as Experiment 3, but used a β-plane rather than an f-plane. As in the previous experiments, eddies initially developed between days 40 to 50. The location of the formation of these eddies (not shown), as in Experiment 2, extended a little farther north in this β-plane experiment than in the f-plane Experiments 1 and 3. Surface contour plots of instantaneous velocity, temperature and dynamic height for day 90 are shown in Figure 14. The zonal (Fig. 14a) and meridional (Fig. 14b) velocities vary between ~5 and 15 cm s^{-1}. A comparison of the dynamic height field (Fig. 14c) and the sea surface temperature field (Fig. 14d) shows, as in previous experiments, that the isotherm perturbations align with the offshore/onshore (geostrophic) flow of the eddies, consistent with CCS observations of squirts (Davis, 1985).

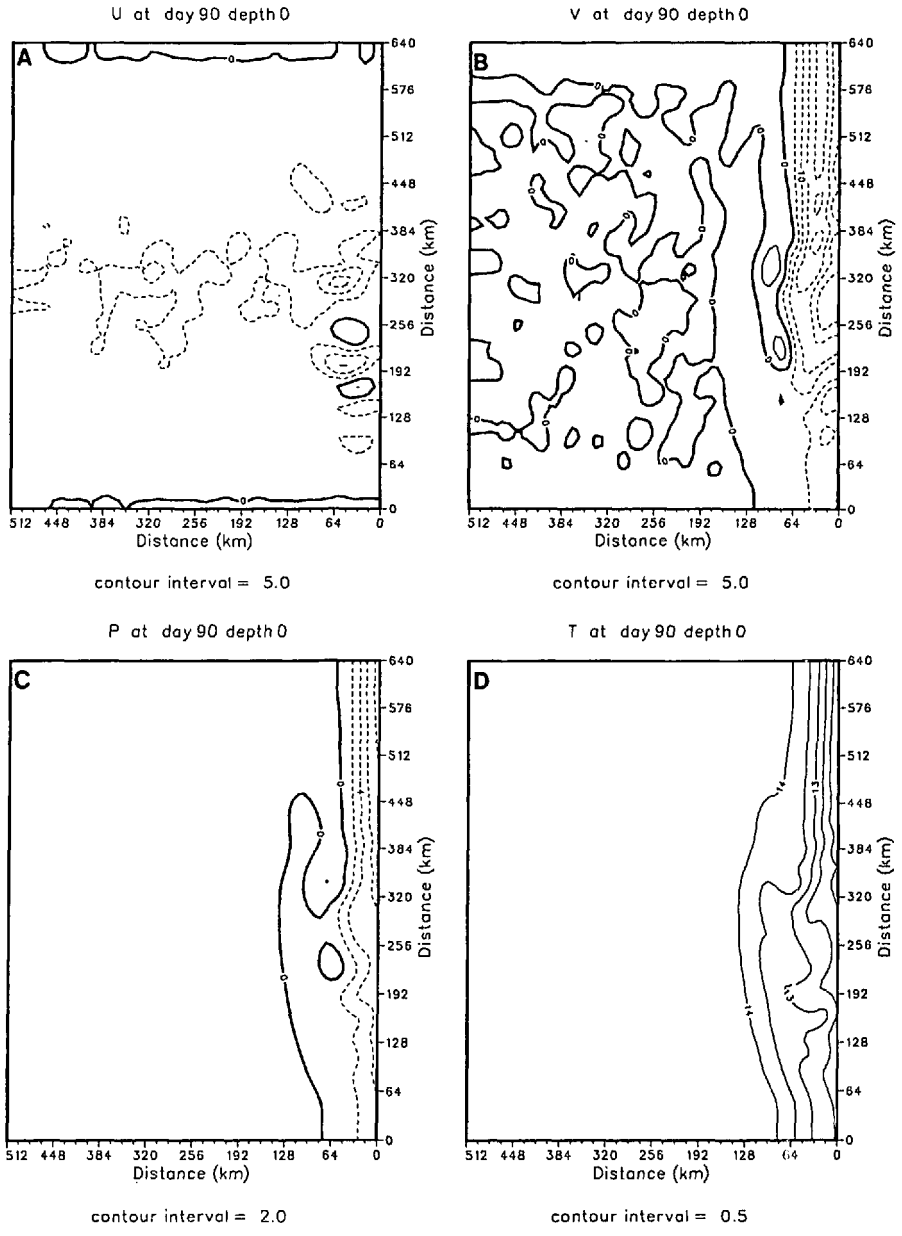

Figure 13. Same as Figure 8 except for Experiment 3.

Of particular interest is the north-south extent of the perturbation fields. A comparison of the zonal velocity fields at day 90 for this experiment (Fig. 14a) and Experiment 3 (Fig. 13a) shows that both the Beta effect and the variation in alongshore wind stress can affect the location of the eddy development region. On an f-plane, when the variation in alongshore wind stress is included, eddies are preferen-

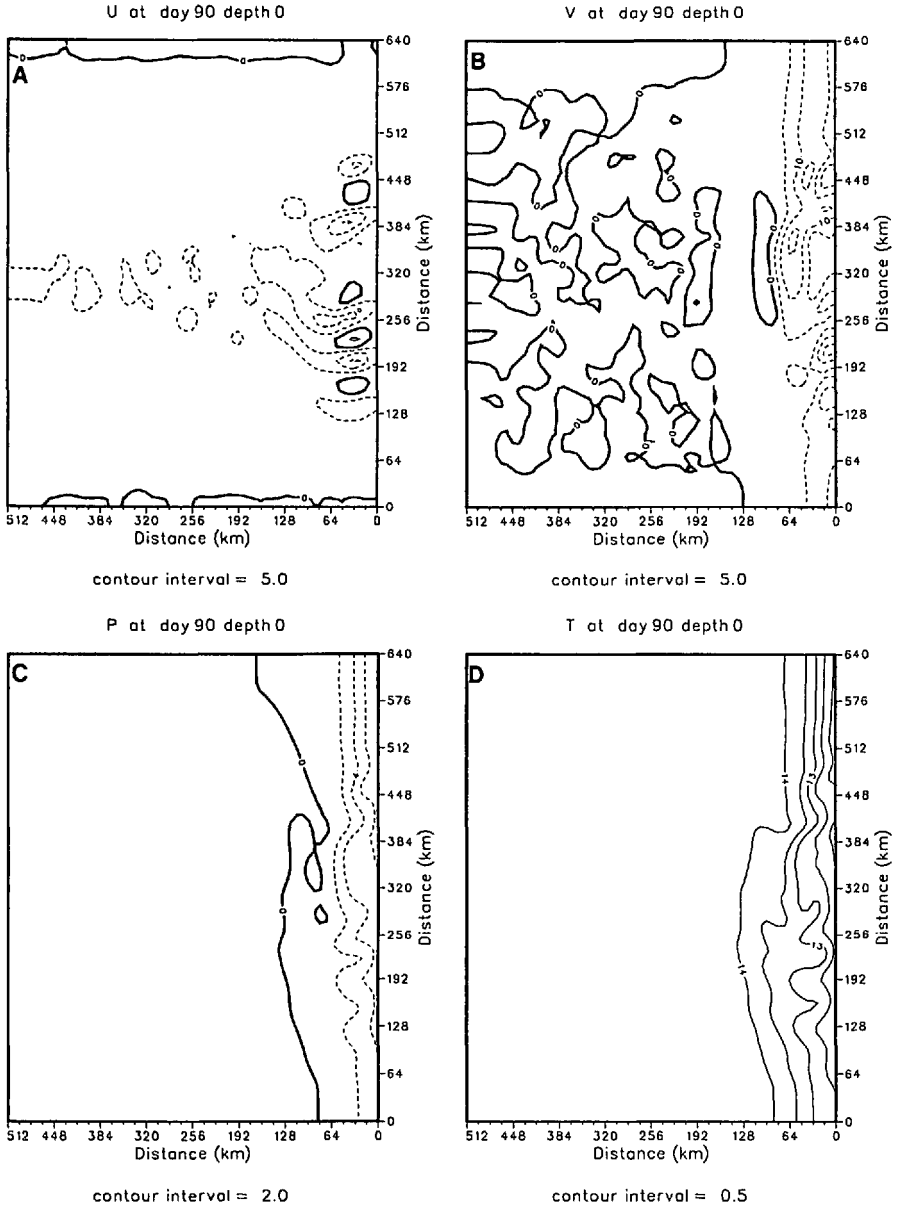

Figure 14. Same as Figure 8 except for Experiment 4.

tially generated in and to the south of the area of maximum alongshore wind stress (compare Fig. 8a with Fig. 13a). With the addition of the Beta effect, eddies also appear to the north of this area (Fig. 14a). Because of the inclusion of both alongshore-varying wind stress and the β-plane, the results of this experiment should be more representative of the observed flow in the CCS than the other experiments.

4. Stability analysis

The dynamical reasons for the generation of the eddy and jet patterns in the above experiments will be investigated here. First, we examine the necessary conditions to determine the potential for the flow field to become unstable and generate eddies and jets. It is known that barotropic instability can occur in an f-plane jet if the curvature of the velocity profile changes sign (Haltiner and Williams, 1980). In addition to barotropic instability, baroclinic instability could also be significant due to the available energy from the vertical shear of the coastal jet and undercurrent. Watts (1983) and Watts and Johns (1982) examined the distribution of potential vorticity in the Gulf Stream as a signature of instability. A necessary condition for baroclinic instability to occur is that the cross-stream derivative of potential vorticity change sign somewhere within the domain. In addition, the product of the cross-stream derivative and the basic current is required to be positive. Finally, the coastal jet must meet the requirement for linearization of a basic state current that is slowly changing in space and time (Robinson, 1983); this requirement is met by the structure of the coastal jet in this study.

Watts (1983) examined the potential vorticity (q) signature in the Gulf Stream using the following expression:

$$q \sim (f + \zeta)\frac{\partial T}{\partial z} - \frac{\partial T}{\partial x}\frac{\partial v}{\partial z} \tag{13}$$

where

$$\zeta = \frac{\partial v}{\partial x} - \frac{\partial u}{\partial y}. \tag{14}$$

Following Watts, we similarly studied the coastal jet to determine its potential for instability. A cross-section plot of the time-averaged (days 30–40) potential vorticity (Fig. 15a) for Experiment 1 showed the tendency for potential vorticity to be uniform along isothermal surfaces and to change vertically, consistent with the offshore temperature stratification. The time-average over days 30 to 40 was chosen because it was the period during which the instability occurred. The range of the potential vorticity was between $0.0–2.2 \times 10^{-6}$ °C m^{-1} s^{-1} offshore of the coastal jet. A relative minimum existed in the surface layer of the offshore region due to weak stratification from turbulent vertical mixing. Strong upwelling in the nearshore region caused weak stratification and deeper minimum values there. A relative maximum of potential vorticity was located at a depth of ~100 m, and at distances greater than 63 km offshore, which corresponded to the "seasonal" thermocline in the model. All experiments in this study, where instability occurred, showed similar potential vorticity patterns, and so will not be shown here.

The cross-stream derivative of potential vorticity was plotted (Fig. 15b) by first calculating the horizontal derivative ($\partial q/\partial x$) and then multiplying by one grid length

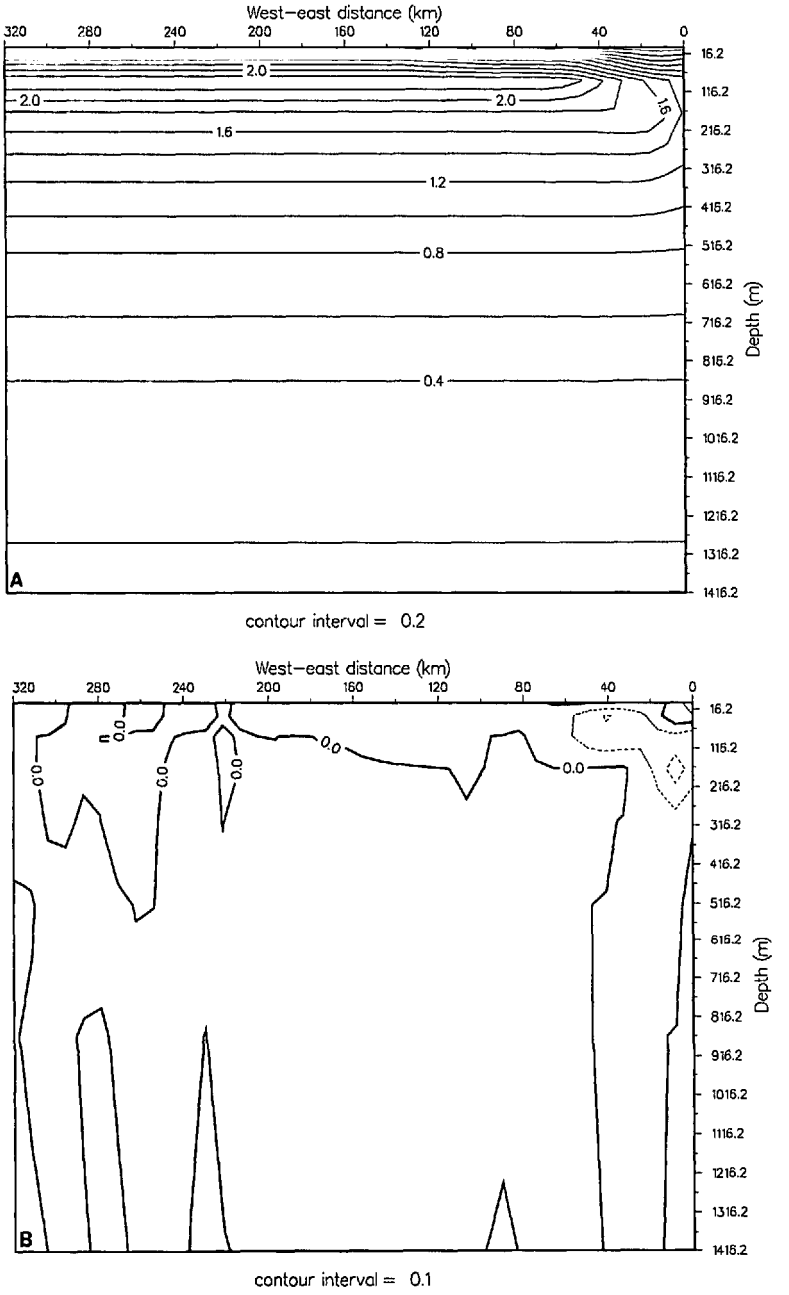

Figure 15. Vertical cross-section of (A) potential vorticity (°C m^{-1} s^{-1}) scaled by 10^6, and (B) the cross-stream derivative of potential vorticity multiplied by the grid size (°C m^{-1} s^{-1}) also scaled by 10^6, for the time-averaged days 30–40 of Experiment 1. Contour interval is 0.2 °C m^{-1} s^{-1} in (A) and 0.1 °C m^{-1} s^{-1} in (B). Dashed contours in (B) denote negative values. The vertical cross-sections were alongshore-averaged.

(Δx). From Figure 15b, it is obvious that the cross-stream derivative meets the necessary condition (of a sign change) for baroclinic instability in the vicinity of the coastal jet and undercurrent, and for barotropic instability in the vicinity of the offshore region of the coastal jet.

In addition to satisfying the necessary condition for instability, it is useful to determine the sufficient conditions for instability. The simple quasigeostrophic two-level model of a uniform baroclinic jet (Holton, 1979) predicts that all waves with an alongshore wave number $k < \sqrt{2}\lambda$ where $\lambda^{-1} = N_o H^*/f_o$ is the Rossby radius of deformation, N_o is the buoyancy frequency and H^* is the interfacial depth, are baroclinically unstable with a growth rate given by

$$\delta = k V_T \left[\frac{2\lambda^2 - k^2}{2\lambda^2 + k^2}\right]^{1/2}. \tag{15}$$

Note that δ depends on λ and on the vertical shear $V_T = \frac{1}{2}(V_1 - V_2)$, where V_1 and V_2 are the upper and lower level currents, respectively. The growth rate, δ, is also a function of k, and is a maximum at an intermediate wavenumber somewhat smaller than $\sqrt{2}\lambda$. Using $H^* = 150$ m, $N_o = 4.7 \times 10^{-3}\,\mathrm{s}^{-1}$, and $V_T = 4\,\mathrm{cm\,s}^{-1}$ as representative of the jet in Experiment 1 for days 30–40, we find that $\lambda^{-1} = \sim 7$ km, and that all waves longer than ~30 km are unstable. The most unstable wave (computed from (15)) has a wavelength of ~50 km and an e-folding time of ~3.5 days. The shortest e-folding time indicates that eddy development should be apparent within a week or so of model integration, after this unstable state has been achieved. Note that these values of the e-folding times and the wavelength of maximum growth rate are only rough approximations to the true values due to the limited applicability of the two-level analysis to the continuous model.

In addition to a stability analysis of the mean flow, it is necessary to examine model heat and momentum diffusion and its associated damping (e-folding) time scale. If the damping time for diffusion is less than the e-folding time due to baroclinic instability, baroclinic instability can be suppressed.

Biharmonic heat and momentum diffusion, as described in Section 2, are used in the PE model. Following the analysis of Holland and Batteen (1986) for a quasigeostrophic (QG) model, the diffusive terms in the thermal vorticity equation can be shown to have the form:

$$(\nabla^2 - \lambda^2)\psi_t = \cdots - A\nabla^6\psi + \lambda^2 K\nabla^4\psi, \tag{16}$$

where ψ is QG "temperature" ($\psi_1 - \psi_3$ in a two layer model), A is the biharmonic eddy viscosity, K is the biharmonic eddy heat diffusion coefficient, and λ^{-1} is the Rossby radius of deformation as before. Assuming wave numbers (k, l), (16) becomes:

$$\psi_t = -\left[\frac{A(k^2 + l^2)^3 + \lambda^2 K(k^2 + l^2)^2}{k^2 + l^2 + \lambda^2}\right]\psi, \tag{17}$$

with solution

$$\psi = \psi_o e^{-\gamma t}. \tag{18}$$

The e-folding (damping) time of baroclinic modes is therefore:

$$\gamma^{-1} = \frac{(k^2 + l^2 + \lambda^2)}{A(k^2 + l^2)^3 + \lambda^2 K(k^2 + l^2)^2} \tag{19}$$

If $A = K$, as in the PE model, the dependence of γ^{-1} on λ drops out and (19) becomes

$$\gamma^{-1} = \frac{1}{A(k^2 + l^2)^2}. \tag{20}$$

Using $A = K = 2 \times 10^{17}$ cm^4 s^{-1}, an alongshore wavelength of 75 km, and a cross-shore wavelength of 130 km (from Fig. 8a), Eq. (20) yields $\gamma^{-1} \sim 65$ days. Since the shortest e-folding time due to baroclinic instability was previously shown to be 3.5 days, diffusive damping would appear to be fairly negligible compared with the baroclinic growth rate. For longer wavelengths, which also experience some growth due to baroclinic instability, the diffusive damping is entirely negligible.

Stability analysis of the other experiments was also made. Experiment 3, which included the alongshore-varying wind stress on an f-plane, had similar stability results as Experiment 1 due to the interaction of the coastal jet and undercurrent.

For a meridional flow, as in this study, Olivier (1987) demonstrated that there is a difference in flow behavior between a non-zonal and zonal flow on a β-plane. In particular, energy can be released without any component of β acting on it; therefore, any vertical shear above the dissipation level may produce instability.

Instability did occur in the β-plane Experiments 2 and 4. Both of these experiments produced an equatorward coastal jet overlying a poleward undercurrent, with the subsequent development of eddies and jets. These, along with the previous experiments, provide evidence that the generation of complex eddy and jet patterns could be attributed to the instability created by the shear between the coastal jet and the poleward undercurrent.

5. Comparison of model results with observations

Hickey (1979) and Huyer (1983) described the classical features of the CCS as consisting of a baroclinic alongshore coastal upwelling jet with the strongest flow at the surface over the midshelf or outer shelf and a poleward undercurrent over the shelf break. In other investigations (Bernstein *et al.*, 1977; Mooers and Robinson, 1984; Rienecker *et al.*, 1985, 1988; Davis, 1985; Kosro and Huyer, 1986; Kosro, 1987; Huyer and Kosro, 1987 and Lynn and Simpson, 1987), the instantaneous near-surface currents often deviated substantially from the time-averaged, classical picture. In particular, Kosro (1987) examined synoptic maps of the coastal current field off northern California during CODE (Coastal Ocean Dynamics Experiment) and found

Table 2. Time-averaged comparison of model experiments (exp.) with observations (obs.) of the CCS.

	Obs.	Exp. 1	Exp. 2	Exp. 3	Exp. 4
A. Maximum coastal jet velocity (cm s^{-1})	5–20 (1, 2, 3, 4, 5)	14	12	14	12
B. Offshore location of coastal jet (km)	15–30 (1, 2)	20–25	20–25	20–25	20–25
C. Offshore extent of coastal jet (km)	>40 (1, 2)	70	60	60	75
D. Depth of inshore coastal jet (m)	90–130 (1, 2, 3)	150	130	150	140
E. Maximum vertical shear of coastal jet ($\times 10^{-3}$ s^{-1})	<2.5 (1, 2)	.9	.9	.9	.9
F. Maximum undercurrent velocity (cm s^{-1})	5–10 (1, 2, 3, 4)	2	4	2	4
G. Offshore location of undercurrent axis (km)	<30 (1, 2, 4)	10	10	10	10
H. Maximum width of undercurrent (km)	10–20 (1, 2)	10–20	20–25	15–20	20–25
I. Depth of undercurrent axis (m)	>200 (1, 2, 3, 4)	300	300	300	300

References: (1) Chelton (1984)
(2) Huyer and Kosro (1987)
(3) Hickey (1979)
(4) Lynn and Simpson (1987)
(5) Davis (1985)

a qualitative correlation between complex temperature patterns in satellite imagery and intense current structures such as squirts, jets and eddies. The distance of these features from shore and their intensity also varied greatly. Davis (1985) investigated CODE drifting buoy data and concluded that it was misleading to think of the California coastal circulation as a simple wind-driven alongshore current with cross-shelf Ekman-driven circulation; instead, he found that various mesoscale features could be the primary mechanisms for cross-shelf transport.

A comparison of model results with available observations was carried out to see if both time-averaged and instantaneous model simulations of the coastal jet, undercurrent and eddies were consistent with the observed data. The time-averaged (over days 30 to 40) comparisons, prior to the generation of eddies, are shown in Table 2, while the instantaneous comparisons (taken at day 90) to highlight specific characteristics of the currents and eddies are shown in Table 3. The time-averaged results from Figure 27 (bottom) of Huyer and Kosro (1987) were obtained from a set of synoptic data during CODE that included both strong wind events and periods of wind relaxation. These observations may not be representative of longer term average climatological conditions in the CCS. Chelton's (1984) study, which shows generally weaker mean flows, is more representative of long term means.

Table 3. Instantaneous comparison of model experiments (exp.) with observations (obs.) of the CCS.

	Obs.	Exp. 1	Exp. 2	Exp. 3	Exp. 4
A. Maximum coastal jet velocity (cm s^{-1})	30–80 (1, 2, 3, 4)	20	15	20	15
B. Offshore location of coastal jet (km)	25–35 (2, 3)	25–35	25–35	25–35	25–35
C. Offshore extent of coastal jet (km)	>40 (1, 2, 3)	70	75	70	75
D. Depth of inshore coastal jet (m)	90–150 (2, 3)	150	140	150	140
E. Maximum vertical shear of coastal jet ($\times 10^{-3}$ s^{-1})	<2.9 (2, 3)	.8	.9	.8	.9
F. Maximum undercurrent velocity (cm s^{-1})	5–15 (2, 3)	6	4	4	4
G. Offshore location of undercurrent axis (km)	10–40 (2, 3)	10	10	10	10
H. Maximum width of undercurrent (km)	10–20 (2, 3)	15	20–30	15	20–25
I. Depth of undercurrent axis (m)	200–300 (2)	300	300–330	300	300–330
J. Maximum zonal eddy diameter (km)	10–100 (2, 5)	50	60	50	60
K. Maximum zonal eddy velocity (cm s^{-1})	50–80 (1, 2, 3, 4)	20	20	20	20

References:
(1) Kosro and Huyer (1986)
(2) Huyer and Kosro (1987)
(3) Kosro (1987)
(4) Davis (1985)
(5) Mooers and Robinson (1984)

As shown by Table 2, there is very little difference in the results of the four model experiments, which compare quite favorably with the mean conditions in the CCS. The only discrepancies are that the simulated coastal jet is slightly deeper than in the observations, and the simulated poleward undercurrent is ~5 cm s^{-1} weaker than observations with its axis location ~10 km closer to shore.

These discrepancies could be due to the model choices of a flat bottom rather than a shelf/slope topography, steady rather than transient wind forcing, neglect of salinity, and/or the particular climatological temperature profile used for the initial mean stratification. The presence of a shelf/slope topography could displace the axis location of both the coastal jet and undercurrent closer to shore. In addition, transient rather than steady wind forcing could result in a more realistic undercurrent (McCreary *et al.*, 1987). Moreover, our value for the average alongshore wind stress for Experiment 1, using data from Nelson (1977), was ~1 dyne cm^{-2}, which was ~33% lower than the calculated values observed by Huyer and Kosro (1987). Our lower value for wind stress would also contribute to a weaker undercurrent than what Huyer and Kosro (1987)

observed. In addition, a stronger initial thermocline (including salinity effects) could perhaps increase and narrow the coastal jet structure.

The instantaneous model results (Table 3) also show good agreement with CCS observations except that the coastal jet, including the offshore-onshore eddy flows, is too weak in the model. Although the instantaneous coastal jet is also somewhat too deep, the model poleward undercurrent is more consistent with the instantaneous observations. The largest difference between the model results and CCS observations is in the maximum eddy velocities. CCS observations from CODE and OPTOMA show eddy velocities of ~50–80 cm s^{-1} while the model shows maximum eddy velocities of only ~20 cm s^{-1}. This discrepancy is attributed to physical factors not included in the model. A prime candidate is the considerable difference between the steady climatological wind stress used to force the model and the stronger and transient wind stress observed during CODE. Other factors that are likely to be important, but which have been neglected in the present focused study, include variations in the coastline and bottom topography.

6. Summary

This study used a high-resolution, multi-level PE ocean model to investigate wind forcing as a possible generation mechanism for mesoscale eddies and jets in the CCS. A band of zonally uniform, steady winds, either with or without alongshore variability, was used as forcing on either an f-plane or a β-plane in an idealized, flat-bottomed oceanic regime along an eastern ocean boundary.

The model results of Experiment 1, which included uniform wind stress on an f-plane, showed the development of an equatorward coastal jet and poleward undercurrent. The coastal jet and undercurrent became unstable after ~40 to 45 days resulting in the generation of eddies and jets. Similar results occurred in Experiment 2, which had the same form of wind stress as in Experiment 1, but used a β-plane rather than an f-plane. However, a comparison of Experiment 2 with Experiment 1 showed that, due to the Beta effect, the coastal jet was shallower and weaker offshore, and the undercurrent stronger and wider in Experiment 2.

The model results of Experiment 3, which had an alongshore-varying wind stress (Fig. 2) on an f-plane, were generally comparable to Experiment 1. However, the variation in alongshore wind stress restricted somewhat the location of eddy development. In particular, the eddies developed in the region of maximum alongshore wind stress, and they were generally confined to the vicinity, and downstream of, the latitude of maximum wind stress. Experiment 4 incorporated an alongshore-varying wind stress, but used a β-plane rather than an f-plane. The fact that eddies developed farther north of the localized eddy generation area of Experiment 3 showed that the Beta effect can also play a role in modifying the location of eddy generation. Because of the inclusion of both alongshore-varying wind stress and the β-plane, the results of

Experiment 4 should be more representative of the dynamics and structure of the CCS than the other experiments.

A comparison of model results with available observations showed that the time-averaged model coastal jet and undercurrent were consistent with available CCS observations (e.g., Huyer and Kosro, 1987) and other model results (McCreary *et al.*, 1987). The time-averaged simulations showed a classical two-dimensional coastal jet. The main discrepancy with observations is that the model eddies were considerably weaker than observed eddies in the CCS.

The results from these experiments strongly support the hypothesis that wind forcing can be a significant generation mechanism for eddies and jets. It should be noted, however, that this study employed the constraints of a regular, straight coastline and a flat bottom in order to isolate and examine the effect of steady wind stress. Future studies will include both an irregular coastline and bottom topography. Time-dependent wind forcing, such as wind events and relaxations, and wind stress with curl experiments are presently being systematically run and investigated to see if transient wind forcing and/or wind stress curl can also be important eddy generation mechanisms.

Acknowledgments. This work was done in the Departments of Oceanography and Meteorology at the Naval Postgraduate School (NPS) under the support of the NPS Research Foundation for Mary Batteen, the Office of Naval Research (ONR) for Robert Haney, and direct funding at NPS for both Mary Batteen and Robert Haney with ONR as the sponsor. Comments by Dr. J. P. McCreary, Jr. on an earlier version of this paper, and by Dr. C. N. K. Mooers, CDR Craig S. Nelson and Ms. A. A. Bird on a later version of this paper, are greatly appreciated. Computer time was provided by the W.R. Church Computer Center at the Naval Postgraduate School.

REFERENCES

Adamec, D., R. L. Elsberry, R. W. Garwood, Jr. and R. L. Haney. 1981. An embedded mixed layer-ocean circulation model. Dyn. Atmos. Oceans, *5*, 69–96.

Arakawa, A. and V. R. Lamb. 1977. Computational design of the basic dynamical processes of the UCLA general circulation model. Methods in Computational Physics, J. Chang, ed., Academic Press, *17*, 173–265.

Batteen, M. L. 1989. Model simulations of a coastal jet and undercurrent in the presence of eddies and jets in the California Current System, *in* Poleward Flows on Eastern Boundaries, S. Neshyba, C. N. K. Mooers, R. L. Smith and R. T. Barber, eds., Lecture Notes on Coastal and Estuarine Studies, Springer-Verlag, 263–279.

Batteen, M. L. and Y.-J. Han. 1981. On the computational noise of finite-difference schemes used in ocean models. Tellus, *33*, 387–396.

Bernstein, R. L., L. C. Breaker and R. Whritner. 1977. California Current eddy formation: ship, air and satellite results. Science, *195*, 353–359.

Blumberg, A. F. and G. L. Mellor. 1987. A description of a three-dimensional coastal ocean circulation model, *in* Three-dimensional Coastal Ocean Models, N. Heaps, ed., American Geophysical Union, *4*, 1–16.

Breaker, L. C. and C. N. K. Mooers. 1986. Oceanic variability off the central California coast. Prog. in Oceanogr., *17*, 61–135.

Camerlengo, A. L. and J. J. O'Brien. 1980. Open boundary conditions in rotating fluids. J. Comput. Physics, *35*, 12–35.

Chelton, D. B. 1984. Seasonal variability of alongshore geostrophic velocity off central California. J. Geophys. Res., *89*, 3473–3486.

Davis, R. E. 1985. Drifter observations of coastal surface currents during CODE: the method and descriptive view. J. Geophys. Res., *90*, 4741–4755.

Emery, W. J. and L. A. Mysak. 1980. Dynamical interpretations of satellite-sensed thermal features off Vancouver Island. J. Phys. Oceanogr., *10*, 961–970.

Feliks, Y. 1985. Notes and correspondence on the Rossby radius of deformation in the ocean. J. Phys. Oceanogr., *15*, 1605–1607.

Flament, P., L. Armi and L. Washburn. 1985. The evolving structure of an upwelling front. J. Geophys. Res., *90*, 11,765–11,778.

Gill, A. E. 1982. Atmosphere-Ocean Dynamics. Academic Press, 662 pp.

Haltiner, G. J. and R. T. Williams. 1980. Numerical Prediction and Dynamic Meteorology, 2nd ed., John Wiley and Sons Inc., 477 pp.

Haney, R. L. 1985. Midlatitude sea surface temperature anomalies: A numerical hindcast. J. Phys. Oceanogr., *15*, 787–799.

Haney, R. L., W. S. Shiver and K. H. Hunt. 1978. A dynamical-numerical study of the formation and evolution of large-scale ocean anomalies. J. Phys. Oceanogr., *8*, 952–969.

Hickey, B. M. 1979. The California Current System—hypothesis and facts. Prog. in Oceanogr., *8*, 191–279.

Holland, W. R. 1978. The role of mesoscale eddies in the general circulation of the ocean—numerical experiments using a wind-driven quasigeostrophic model. J. Phys. Oceanogr., *8*, 363–392.

Holland, W. R. and M. L. Batteen. 1986. The parameterization of subgrid scale heat diffusion in eddy-resolved ocean circulation models. J. Phys. Oceanogr., *16*, 200–206.

Holton, J. R. 1979. An Introduction to Dynamic Meteorology, 2nd ed. Academic Press, 391 pp.

Hurlburt, H. E. and J. D. Thompson. 1973. Coastal upwelling on a beta-plane. J. Phys. Oceanogr., *3*, 16–32.

Huyer, A. 1983. Coastal upwelling in the California Current System. Prog. in Oceanogr., *12*, 259–284.

Huyer, A. and P. M. Kosro. 1987. Mesoscale surveys over the shelf and slope in the upwelling region near Point Arena, California. J. Geophys. Res., *92*, 1655–1681.

Ikeda, M. and W. J. Emery. 1984. Satellite observations and modeling of meanders in the California Current system off Oregon and Northern California. J. Phys. Oceanogr., *14*, 1434–1450.

Kosro, P. M. 1987. Structure of the coastal current field off Northern California during the Coastal Ocean Dynamics Experiment. J. Geophys. Res., *92*, 1637–1654.

Kosro, P. M. and A. Huyer. 1986. CTD and velocity surveys of seaward jets off Northern California, July 1981 and 1982. J. Geophys. Res., *91*, 7680–7690.

Lynn, R. J., K. Bliss and L. E. Eber. 1982. Vertical and horizontal distributions of seasonal mean temperature, salinity, sigma-*t*, stability, dynamic height, oxygen, and oxygen saturation in the California Current, 1950–1978, CalCOFI Atlas 30, State of Calif. Mar. Res. Comm., La Jolla, 513 pp.

Lynn, R. J. and J. J. Simpson. 1987. The California Current System: the seasonal variability of its physical characteristics. J. Geophys. Res., *92*, 947–966.

McCreary, J. P., Jr. 1981. A linear stratified ocean model of the coastal undercurrent. Phil. Trans. Roy. Soc., London, *A 302,* 385–413.

McCreary, J. P., Jr., P. K. Kundu and S.-Y. Chao. 1987. On the dynamics of the California Current System. J. Mar. Res., *45,* 1–32.

Mooers, C. N. K. and A. R. Robinson. 1984. Turbulent jets and eddies in the California Current and inferred cross-shore transports. Science, *223,* 51–53.

Nelson, C. S. 1977. Wind stress and wind stress curl over the California Current. NOAA Tech. Rep. NMFS SSRF-714, U.S. Dept. Commerce, 87 pp.

Nelson, C. S. and D. M. Husby. 1983. Climatology of surface heat fluxes over the California Current Region. NOAA Tech. Rep. NMFS SSRF-763, U.S. Dept. Commerce, 155 pp.

Olivier, D. A. 1987. Numerical simulations of the California Current: filament formation as related to baroclinic instability, Master's Thesis. Naval Postgraduate School, Monterey, CA, 68 pp.

Paulson, C. A. and J. J. Simpson. 1977. Irradiance measurements in the upper ocean. J. Phys. Oceanogr., *7,* 952–956.

Philander, S. G. H. and J.-H. Yoon. 1982. Eastern boundary currents and coastal upwelling. J. Phys. Oceanogr., *12,* 862–879.

Rienecker, M. M., C. N. K. Mooers, D. E. Hagan and A. R. Robinson. 1985. A cool anomaly off Northern California: An investigation using IR imagery and *in situ* data. J. Geophys. Res., *90,* 4807–4818.

Rienecker, M. M., C. N. K. Mooers and R. L. Smith. 1988. Mesoscale variability in current meter measurements in the California Current System off Northern California. J. Geophys. Res., *93,* 6711–6734.

Robinson, A. R. 1983. Eddies in Marine Science, Springer-Verlag, NY, 609 pp.

Robinson, A. R., J. A. Carton, C. N. K. Mooers, L. J. Walstad, E. F. Carter, M. M. Rienecker, J. A. Smith and W. G. Leslie. 1984. A real-time dynamical forecast of ocean synoptic/mesoscale eddies. Nature, *309,* 781–783.

Thomson, R. E. 1984. A cyclonic eddy over the continental margin off Vancouver Island: Evidence for baroclinic instability. J. Phys. Oceanogr., *14,* 1326–1348.

Watts, D. R. 1983. Gulf Stream variability, *in* Eddies in Marine Science, A. R. Robinson, ed., Springer-Verlag, NY, 114–144.

Watts, D. R. and W. E. Johns. 1982. Gulf Stream meanders: Observations on propagation and growth. J. Geophys. Res., *87,* 9467–9476.

Weatherly, G. L. 1972. A study of the bottom boundary layer of the Florida Current. J. Phys. Oceanogr., *2,* 54–72.

Wright, D. G. 1980. On the stability of a fluid with specialized density stratification. Part II. Mixed baroclinic-barotropic instability with application to the Northeast Pacific. J. Phys. Oceanogr., *19,* 1307–1322.

Received: *29 November, 1988;* revised: *6 April, 1989.*